Nano Research
2021, 14(8): 2819–2825
ISSN 1998-0124 CN 11-5974/O4
https://doi.org/10.1007/s12274-021-3292-4

Research Article

Self-templated formation of cobalt-embedded hollow N-doped carbon spheres for efficient oxygen reduction

Ayaz Mahsud[1,§], Jianian Chen[1,§], Xiaolei Yuan[2,§], Fenglei Lyu[1] (✉), Qixuan Zhong[1], Jinxing Chen[1,3], Yadong Yin[3], and Qiao Zhang[1] (✉)

[1] *Institute of Functional Nano & Soft Materials (FUNSOM), Jiangsu Key Laboratory for Carbon-Based Functional Materials & Devices, Joint International Research Laboratory of Carbon-Based Functional Materials and Devices, Soochow University, 199 Ren'ai Road, Suzhou 215123, China*

[2] *School of Chemistry and Chemical Engineering, Nantong University, Nantong, 9 Seyuan Road, Nantong 226019, China*

[3] *Department of Chemistry, Materials Science and Engineering program, and UCR Center for Catalysis, University of California, Riverside, CA 92521, USA*

[§] *Ayaz Mahsud, Jianian Chen, and Xiaolei Yuan contributed equally to this work.*

Received: 13 January 2020 / **Revised:** 15 November 2020 / **Accepted:** 9 December 2020

ABSTRACT

The slow kinetics at the cathode of oxygen reduction reaction (ORR) seriously limits the efficiencies of fuel cells and metal-air batteries. Pt, the state-of-the-art ORR electrocatalyst, suffers from high cost, low earth abundance, and poor stability. Here a self-templated strategy based on metal-organic frameworks (MOFs) is proposed for the fabrication of hollow nitrogen-doped carbon spheres that are embedded with cobalt nanoparticles (Co/HNC). The Co/HNC manifests better ORR activities, methanol tolerance, and stability than commercial Pt/C. The high ORR performance of Co/NHC can be attributed to the hollow structure which provides enlarged electrochemically active surface area, the formation of more Co-N species, and the introduction of defects. This work highlights the significance of rational engineering of MOFs for enhanced ORR activity and stability and offers new routes to the design and synthesis of high-performance electrocatalysts.

KEYWORDS

cobalt, self-templated, metal organic framework, hollow sphere, oxygen reduction reaction

1 Introduction

The increasing energy demand and environment issues brought by the consumption of fossil fuels have stimulated intensive research on clean and sustainable energy technologies, such as fuel cells and metal-air batteries [1–4]. The performance of fuels cells and metal-air batteries is severely limited by the slow kinetics at the cathode of oxygen reduction reaction (ORR). As the state-of-the-art ORR electrocatalyst, Pt suffers from high cost, low earth abundance, and poor stability, which impede its large-scale applications [5, 6]. Developing high-performance Pt-free ORR electrocatalysts with low cost and high abundance is therefore in urgent demand. Over the past decades, tremendous efforts have been devoted to exploring Pt-free ORR electrocatalysts, and significant achievement has been made. For example, various Pt-free electrocatalysts have been developed, including transition-metal-based inorganic nanomaterials (such as metal oxides [7], chalcogenides [8], carbides [9], and nitrides [10]), metal-free nanocarbon [11] and metal-nitrogen/carbon (M-N/C) nanocomposites [12–23].

Among various alternatives, M-N/C (M= Fe and Co) showed great potential in large-scale applications because of their relatively high activity, good stability, and low cost. Despite tremendous efforts and great achievements, the M-N/C-based catalysts still exhibit high over-potentials for ORR. As a typical gas-involving electrocatalytic process, the ORR process involves several steps including mass diffusion of oxygen from electrolyte to the active sites, electron transfer from conductive support to the active sites, and the surface reduction reaction [24]. The challenges associated with M-N/C are their relatively lower intrinsic activity than Pt, poor mass transfer, and limited active sites [25]. According to recent reports, three key components should be realized in M-N/C composites for high ORR performance, including the presence of M-N_x sites, high surface area, and good conductivity. First, a high density of M-N_x sites is crucial in M-N/C composites, because they are generally regarded as the active sites for ORR [26]. Second, a high surface area is required because it ensures efficient mass diffusion to the active sites. Third, the conductivity of the composite is important as it can facilitate the electron transfer.

Metal-organic frameworks (MOFs) have flourished as promising scaffolds for the synthesis of various electrocatalysts because of their abundant source of metal, nitrogen, and carbon [27, 28]. As a subclass of MOFs, cobalt-based zeolitic imidazolate frameworks (ZIFs) are ideal precursors for Co-N/C based ORR electrocatalysts [29–35]. As high-temperature pyrolysis of ZIFs is necessary for the formation of Co-N/C composites, it often leads to severe fusion and aggregation of the active Co-N sites. In this regard, hollow N-doped carbon is highly desirable for enhanced mass diffusion and electron transfer. On the one

Address correspondence to Fenglei Lyu, fllv@suda.edu.cn; Qiao Zhang, qiaozhang@suda.edu.cn

hand, hollow micro/nanostructures have their unique advantages, such as multiple interphases and short mass diffusion lengths, which are beneficial for the exposure of active sites and mass transfer of oxygen [36–38]. On the other hand, N-doping could effectively alter the electronic structure of carbon species, enhance their electric conductivity, and facilitate the fast electron transfer [39].

The self-templating method, which refers to the template materials that are fully or partially converted by the shells during the formation of a hollow structure, is widely applied for the synthesis of hollow-structured nanomaterials [40, 41]. Compared with other methods such as hard- or soft-templating methods, the self-templating method can avoid the heterogeneous coating on the templates [42–44], providing a relatively simple synthesis procedure which has high reproducibility and low production cost [45]. Inspired by the above discussion, here we demonstrate a MOF-engaged self-templated strategy for the synthesis of cobalt-embedded hollow N-doped carbon spheres (Co/HNC). The Co/HNC manifests high ORR activity with half-wave potential ($E_{1/2}$) of 0.83 V and diffusion-limiting current density (j_L) of 5.46 mA·cm^{-2}, which is better than commercial Pt/C ($E_{1/2}$ = 0.82 V and j_L = 5.17 mA·cm^{-2}). In addition, Co/HNC also shows much better methanol tolerance and ORR stability than commercial Pt/C. The high ORR performance of Co/HNC can be attributed to the hollow structure which provides high electrochemically active surface area, the formation of abundant Co-N species, and the introduction of defects.

2 Results and discussion

The formation process of Co/HNCs was schematically illustrated in Fig. 1. In the first step, bimetallic CoZn-glycolate (CoZn-Gly) microspheres were synthesized via a solvothermal method using $Co(NO_3)_2$ and $Zn(NO_3)_2$ in a mixed solvent of ethanol and ethylene glycol (see Experimental Section for details). During the solvothermal process, the hydroxyl group in ethylene glycol can coordinate with Co^{2+} and Zn^{2+} ions, resulting in the formation of CoZn-Gly complex. In the second step, Co^{2+} and Zn^{2+} ions in CoZn-Gly coordinated with 2-methylimidazole (2-MI) and formed a bimetallic ZIF shell on the outside of CoZn-Gly. Finally, the core/shell CoZn-glycolate/bimetallic ZIFs (CoZn-Gly/BMZIF) were calcined under H_2/N_2 atmosphere to obtain cobalt-embedded hollow nitrogen-doped carbon spheres (Co/HNC). During the pyrolysis, the ZIF shell was converted into Co/HNC phase and the evaporation of Zn species in the core led to the formation of void space inside the shells.

The morphologies of CoZn-Gly, CoZn-Gly/BMZIF, and Co/HNC were investigated by scanning electron microscopy (SEM) and transmission electron microscopy (TEM). From the SEM images (Fig. 2(a) and Fig. S1 in the Electronic Supplementary Material (ESM)), the CoZn-Gly showed spherical morphology

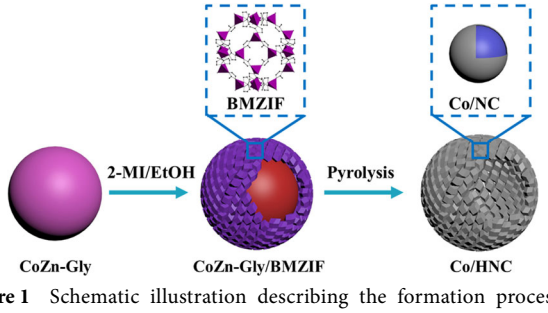

Figure 1 Schematic illustration describing the formation process of Co/HNC.

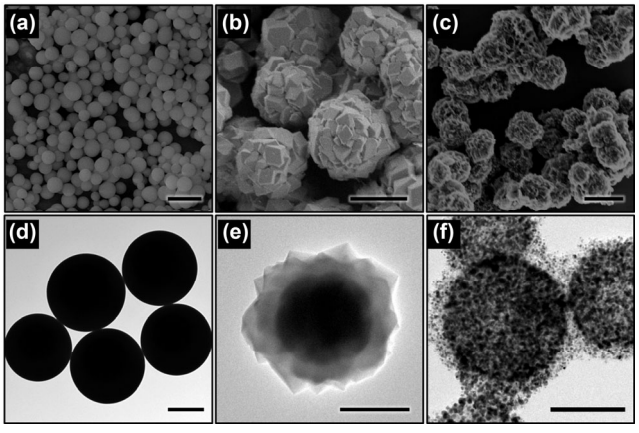

Figure 2 SEM (a)–(c) and TEM (d)–(f) images of (a) and (d) CoZn-Gly, (b) and (e) CoZn-Gly/BMZIF and (c) and (f) Co/HNC-1. Scale bars: 2 μm in (a), 1 μm in (b)–(e), 200 nm in (f).

with smooth surfaces. The solid nature of CoZn-Gly was further revealed by the TEM images (Fig. 2(d)). The particle sizes of CoZn-Gly solid spheres were 2.00 ± 0.15 μm in diameter. CoZn-Gly-0.5 and CoZn-Gly-2 also showed spherical morphology with particle sizes of 2.61 ± 0.35 μm and 0.93 ± 0.22 μm in diameters, respectively. The morphological change was observed owing to the reaction with 2-MI. The surface of CoZn-Gly/BMZIF became rough and rhombic dodecahedral particles were oriented grown on the surfaces of the microspheres (Fig. 2(b)). The well-defined structure with a spherical core (~ 1.35 μm in diameter) and polyhedral shell (~ 0.4 μm in thickness) could be further observed in the TEM image (Fig. 2(e)). After pyrolysis, the Co/HNC maintained the spherical structure with rough surfaces (Fig. 2(c) and Fig. S2 in the ESM). Small nanoparticles distributed in the hollow matrix could be seen in the TEM image of Co/HNC-1 (Fig. 2(f)). Zn has a low boiling point (~ 907 °C) and can evaporate to vapor phase at a high temperature (> 900 °C). The formation of hollow structure could be attributed to the evaporation of Zn during pyrolysis. High-resolution TEM (HRTEM) image of Co/HNC-1 (Fig. S3 in the ESM) further confirmed that cobalt nanoparticles were encapsulated in the graphitic carbon shells, in which the interplanar spacing of wrapped nanoparticle (0.204 nm) and the outer layer (0.334 nm) could be indexed as the (111) plane of metallic cobalt and the (002) plane of graphitic carbon, respectively. The formation of metallic cobalt and graphitic carbon could be attributed to the carbonization of 2-MI linker and the *in situ* reduction of Co^{2+}. The distribution of different element was further revealed by high-angle annular dark-field scanning transmission electron microscopy (HAADF-STEM), in which C, N, Co and Zn element overlapped well with the STEM image, suggesting the uniform distribution of these elements (Fig. S4 in the ESM).

The phases of CoZn-Gly and CoZn-Gly/BMZIF were further examined using X-ray diffraction (XRD). From the XRD patterns (Fig. 3(a) and Fig. S5 in the ESM), no obvious diffraction peaks were detected for CoZn-Gly, indicating its amorphous nature. The CoZn-Gly/BMZIF showed strong diffraction peaks which matched well with the simulated XRD pattern of ZIF, suggesting the formation of zeolite-type shells with high crystallinities. After pyrolysis, diffraction peak for Co/HNC (Fig. 3(b) and Fig. S6 in the ESM) around 26.2° was indexed to the (002) plane of graphitic carbon and peaks at 44.5°, 51.8° and 75.9° can be assigned to the (111), (200) and (220) planes of metallic cobalt (PDF No. 89-4307), in agreement with the HRTEM results. No peaks for metallic Zn were observed in the XRD pattern because of its evaporation during

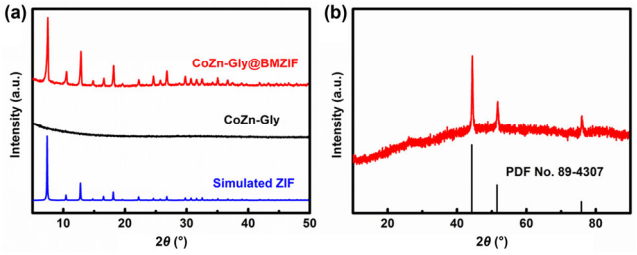

Figure 3 XRD patterns of (a) CoZn-Gly and CoZn-Gly/BMZIF and (b) Co/HNC-1.

pyrolysis. The composition of Co/HNC-1 was further analyzed by the X-ray photoelectron spectra (XPS) survey scan, in which C, N, O, and Co elements could be detected (Fig. S7 in the ESM). The oxygen peak may derive from the surface oxidation because of the exposure to the air atmosphere. High-resolution C 1s XPS spectrum (Fig. S8 in the ESM) could be deconvoluted into four peaks, which were attributed to four types of carbon species, namely C–C (284.6 eV), C–N (285.6 eV), C–O (286.9 eV) and π–π* (290.4 eV), further verifying the presence of N element [15]. By combining the TEM, HRTEM, XRD, and XPS results, one can confirm that cobalt-embedded hollow nitrogen-doped carbon spheres were successfully prepared.

The ORR activity of different samples was evaluated in three-electrode system using catalysts covered glassy carbon, graphitic rod, saturated calomel electrode (SCE), O_2-saturated 0.1 M KOH as the working electrode, counter electrode, reference electrode, and electrolyte, respectively [46–48]. The Co/HNC with different Co and Zn amounts (Co/HNC-0.5, Co/HNC-1, Co/HNC-2), ZIF-67 derived Co-N/C (ZIF-950), and commercial Pt/C were also tested for comparison. From the linear sweep voltammetry (LSV) curves (Fig. 4(a)), ZIF-950 showed the highest overpotential and lowest diffusion-limiting current density among the samples. TEM characterization (Fig. S9 in the ESM) indicated severe aggregation in ZIF-950, which led to

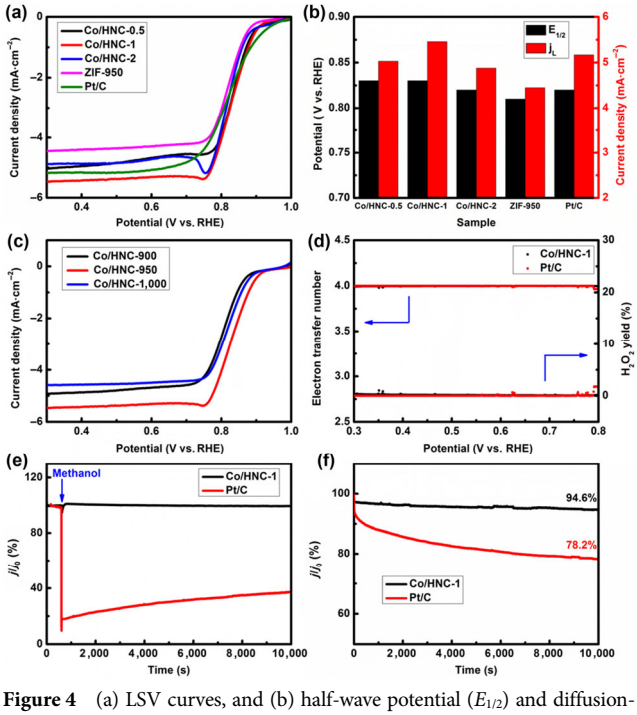

Figure 4 (a) LSV curves, and (b) half-wave potential ($E_{1/2}$) and diffusion-limiting current density (j_L) of Co/HNC-0.5, Co/HNC-1, Co/HNC-2, ZIF-950 and Pt/C. (c) LSV curves of Co/HNC-900, Co/HNC-950, Co/HNC-1,000. (d) Electron transfer number of Co/HNC-1 and Pt/C. (e) Methanol crossover test of Co/HNC-1 and Pt/C. (f) Stability test of Co/HNC-1 and Pt/C.

the reduced active sites and poor ORR activity. The Co/HNC-1 manifested the lowest overpotential and the highest diffusion-limiting current density among all the samples. The half-wave potential ($E_{1/2}$) and the diffusion-limiting current density (j_L) were applied to evaluate the ORR activities (Fig. 4(b)). The Co/HNC-1 had the $E_{1/2}$ of 0.83 V and j_L of 5.46 mA·cm^{-2}, which was higher than that of commercial Pt/C (with $E_{1/2}$ = 0.82 V and j_L = 5.17 mA·cm^{-2}). The ORR activity of the Co/HNC-1 also depended on the pyrolysis temperature. The Co/HNC-1 obtained at 950 °C showed the highest activity among the samples prepared at different pyrolysis temperatures (Fig. 4(c)). A typical LSV curve showed two regions, including the kinetic-controlled region at a low current density and the diffusion-controlled region at a high current density. The kinetics of different samples was evaluated by the Tafel plots (Fig. S10 in the ESM). Co/HNC-1 showed a Tafel slope of 63 mV·dec^{-1}, which was lower than those of Co/HNC-2 (67 mV·dec^{-1}), ZIF-950 (72 mV·dec^{-1}) and Pt/C (90 mV·dec^{-1}), suggesting that Co/HNC-1 had the fastest ORR kinetics among different samples. The high ORR activity also made Co/HNC-1 among one of the best recently reported cobalt-based ORR electrocatalysts in alkaline media (Table S1 in the ESM).

The ORR pathway in alkaline media could be divided into the direct four-electron pathway in which O_2 was reduced into OH^- or the two-electron pathway in which O_2 was reduced into H_2O_2. For the application in fuel cells, the formation of H_2O_2 was not desired because it can destroy the membrane and deteriorate the performance of fuel cells. To investigate the ORR pathway in Co/HNC-1 and Pt/C, we utilized the rotating-ring disk electrode (RRDE) technique (Fig. 4(d)) [49]. The calculated electron transfer number for Pt/C was about 4 because commercial Pt/C was well-known for its four-electron pathway for ORR. The yield of H_2O_2 was less than 2% for Co/HNC-1, and its electron transfer number was more than 3.95, indicating that the Co/HNC-1 followed the direct four-electron pathway and the formation of H_2O_2 was much prohibited.

The resistance to methanol was another important parameter for ORR electrocatalysts in direct methanol fuel cells. The tolerance against methanol crossover was evaluated by injection of methanol during the chronoamperometric test. Upon the injection of methanol, a significant current drop in Pt/C was observed, indicating the poor methanol tolerance of Pt/C. In contrast, there was no obvious current drop for Co/HNC-1, suggesting the excellent resistance to methanol for Co/HNC-1 (Fig. 4(e)). For practical applications, long-term stability is also crucial. From the chronoamperometric curves of Co/HNC-1 and Pt/C (Fig. 4(f)), 94.6% of the original current could be maintained for Co/HNC-1 after 10,000 s, which was larger than that of Pt/C (78.2 %), suggesting better stability of Co/HNC-1. The high ORR activity, low yield of H_2O_2, excellent resistance to methanol, and good stability of the sample may provide a great opportunity for fuel-cell applications.

To get a deeper insight into the high ORR activity of Co/HNC-1, we evaluated the surface areas of Co/HNC-1 and ZIF-950 based on the nitrogen adsorption-desorption isotherms (Fig. 5(a)). Both samples showed a steep increase at low pressure and hysteresis loops at high pressure, which can be ascribed to the presence of both micropores and mesopores. The Brunauer-Emmett-Teller (BET) surface area and pore volume of Co/HNC-1 were measured at 195 m^2·g^{-1} and 0.27 m^3·g^{-1}, which was larger than those of ZIF-950 (175 m^2·g^{-1} and 0.23 m^3·g^{-1}). The mesoporous structure was further confirmed in the pore size distribution plots based on the desorption curves, in which Co/HNC-1 and ZIF-950 showed mesopores

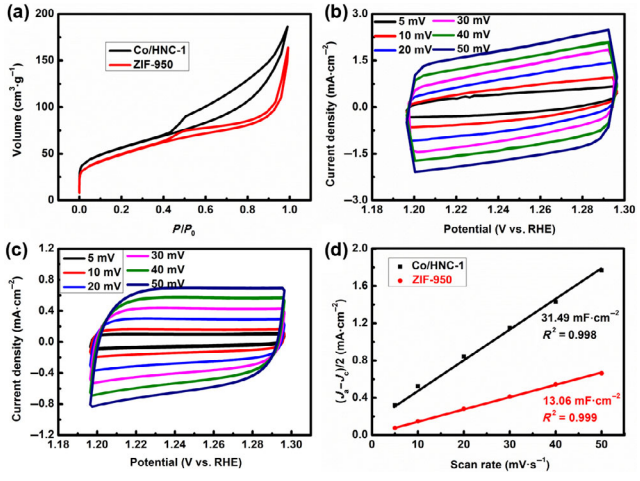

Figure 5 (a) Nitrogen adsorption-desorption isotherms of Co/HNC-1 and ZIF-950. CV curves of Co/HNC-1 (b) and ZIF-950 (c). ECSA of Co/HNC-1 and ZIF-950.

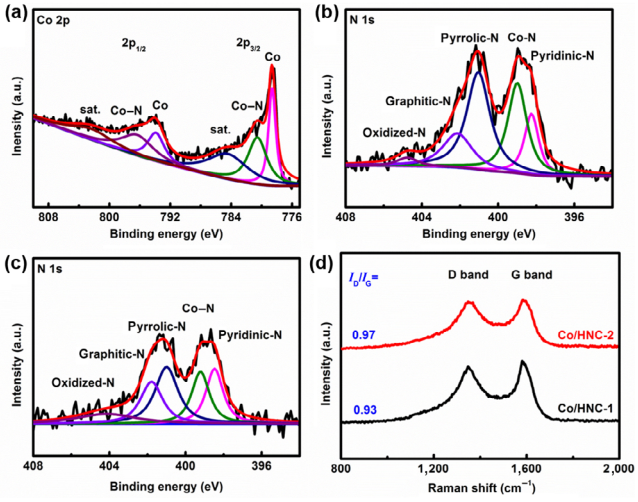

Figure 6 (a) Co 2p XPS spectrum of Co/HNC-1. (b) N 1s spectra of Co/HNC-1. (c) N 1s spectra of Co/HNC-2. (d) Raman spectra of Co/HNC-1 and Co/HNC-2.

with diameters of 3.9 and 3.6 nm, respectively (Fig. S11 in the ESM). The abundant mesopores could serve as the reaction regions for the gas-liquid-solid tri-phase ORR. In addition, the electrochemically active surface areas (ECSA) of Co/HNC-1 and ZIF-950 were estimated using the cyclic voltammetry (CV) method in non-Faradic region (Figs. 5(b) and 5(c)) [50]. The CV curves of Co/HNC-1 and ZIF-950 showed quasi-rectangular shapes and the current densities increased in proportion with the scan rate, suggesting their double-layer capacitance profile (Fig. 5(d)). The slope of Co/HNC-1 was 31.49 mF·cm^{-2}, which was larger than that of ZIF-950 (11.02 mF·cm^{-2}). The larger slope of Co/HNC-1 indicated its higher ECSA than ZIF-950, which could be attributed to its hollow structure that provided multiple interfaces and more exposed active sites.

The surface chemistry of Co/HNC-1 was further investigated by using XPS to gain better understanding of its high ORR activity. The high-resolution Co 2p XPS spectrum (Fig. 6(a), Figs. S12 and S13 in the ESM) of Co/HNC-1 was deconvoluted into $2p_{3/2}$ and $2p_{1/2}$ of metallic Co (778.5/794.1 eV) and Co-N species (780.6/796.5 eV) [35, 51]. The high-resolution N 1s spectrum was deconvoluted into pyridinic-N (398.2 eV), Co-N (399.0 eV), pyrrolic-N (401.1 eV), graphitic-N (402.2 eV), and oxidized-N (404.8 eV) [33]. In previous report, Yao et al. demonstrated that in the core-shell Co@C system, the removal of Co nanoparticles by combining acid washing and electrochemical treatment, in which only single Co species coordinated with the nitrogen in the carbon layers (Co-N) existed, did not affect the ORR performance of the resulting sample [52]. Bao et al. reported that encapsulated Co nanoparticles in Co@CoNC could improve the efficiency and accelerate the ORR reaction by improving the interfacial electron transfer kinetics [53]. Yang et al. demonstrated that the introduction of Co core nanoparticles lowered the d band center of surface Co atoms in graphite shells and made the free energy diagrams of the ORR process on Co-N-C shell more close to the ideal case [54]. In the Co/HNC composites, the Co-N species presumably served as the main active sites for ORR, while the metallic Co nanoparticles acted as the promoter. The Co/HNC-1 had higher Co-N content (28.4%) than that of Co/HNC-2 (19.7%), indicating the presence of more active sites in Co/HNC-1, which was crucial for better ORR activity (Figs. 6(b) and 6(c) and Table S2 in the ESM). After ORR test, the $2p_{3/2}$ and $2p_{1/2}$ orbitals of metallic Co and Co-N species in Co/HNC-1 were detectable (Fig. S14 in the ESM), implying that the Co/HNC is relatively stable during ORR. Furthermore, from the Raman spectrum of Co/HNC-1 and Co/HNC-2 (Fig. 6(d)), peaks around 1,586 cm^{-1} were attributed to the in-plane vibration of sp^2 carbon (G band), and peaks around 1,350 cm^{-1} reflected the structural defect in graphitic carbon [55]. The intensity between D band and G band (I_D/I_G) for Co/HNC-1 and Co/HNC-2 were 0.93 and 0.97, respectively. The lower I_D/I_G indicated the formation of more defects in Co/HNC-1, which changed the local electronic structure of carbon and enhanced its catalytic activity towards ORR [56].

For large-scale applications, Co-N/C based ORR electrocatalysts should be synthesized using cost-effective and straightforward methods with high surface area, abundant active sites, and good stability. In terms of the synthesis, the MOF-based self-templated method is simple, robust, and low cost. Benefiting from the hollow structure, Co/HNC-1 showed high surface area with mesoporosity, leading to enlarged ECSA and more exposed active sites. Furthermore, the hollow structure could enhance the matter transfer of charges and molecules [57–59]. The incorporation of Zn brought the spatial isolation of cobalt to suppress its sintering, further favored the formation of more Co-N species and defects, which facilitated the high ORR activity and fast ORR kinetics. In addition, the Co/HNC-1 also manifested better catalytic stability and tolerance to methanol crossover. The simple synthetic method, high ORR activity and stability made Co/HNC promising candidates for the application in renewable energy devices such as direct methanol fuel cells.

3 Conclusions

In summary, we have demonstrated a MOF-based self-templated strategy for the synthesis of Co/HNC. The Co/HNC manifested better ORR activity, methanol tolerance, and stability than commercial Pt/C. The high ORR performance of Co/HNC could be attributed to the hollow structure which provided larger ECSA, the formation of more active Co-N species, and the introduction of defects. This work highlighted the importance of rational engineering MOFs for enhanced electrocatalytic performance, providing excellent opportunities in the design and synthesis of nanostructured electrocatalysts for energy conversion and storage.

4 Experimental section

Synthesis of CoZn-Gly: In a typical synthesis, 1 mmol $Co(NO_3)_2$

and 1 mmol $Zn(NO_3)_2$ were dissolved in 40 mL ethanol and ethylene glycol (V_{EtOH}/V_{EG}=1:4.5). Then the solution was transferred into a 100-mL autoclave and sealed. After reaction at 180 °C for 12 h, the pink product was centrifuged, washed with ethanol three times, and dispersed in 20 mL ethanol.

Synthesis of CoZn-Gly@BMZIF: 10 mL CoZn-Gly dispersion was mixed with 30 mL 2-methylimidazole (6 g) ethanol solution with the assistance of sonication. Then the mixture was reacted at 100 °C for 3 h in an autoclave. The CoZn-Gly@BMZIF was centrifuged, washed with ethanol, and dried in a vacuum oven at 60 °C.

Synthesis of Co/HNC: Co/HNC-1 was obtained by calcining the CoZn-Gly/BMZIF at 950 °C for 2 h under H_2/N_2 (5% H_2) atmosphere. Co/HNC-0.5 (0.5 mmol Co^{2+} and 1.5 mmol Zn^{2+}) and Co/HNC-2 (2 mmol Co^{2+}) were synthesized using the same procedure as Co/HNC-1 except that different amounts of $Co(NO_3)_2$ and $Zn(NO_3)_2$ were added during the synthesis.

Synthesis of ZIF-950: ZIF-67 was first synthesized according to the literature [60]. Then ZIF-950 was prepared by calcining the ZIF-67 at 950 °C for 2 h under H_2/N_2 (5% H_2) atmosphere.

Characterization: The morphology of the samples was investigated using scanning electron microscopy (Zeiss G500) and transmission electron microscopy (FEI Tecnai F20). Powder XRD patterns were obtained with a PANalytical X-ray diffractometer. XPS spectra were collected on an SSI S-Probe XPS spectrometer. Raman spectra were obtained on a LabRAM HR800 Raman microscope. Nitrogen adsorption-desorption isotherms were collected using a gas sorption system (ASAP2020 HD88). All electrochemical measurements were carried out in a three-electrode cell at room temperature, with a graphitic rod, a saturated calomel electrode (SCE), and 0.1 M KOH as the counter electrode, reference electrode, and electrolyte, respectively. For the preparation of the working electrode, 5 mg of catalysts were dispersed in 750 μL water, 250 μL isopropanol, and 50 μL Nafion solution (5%) with the assistance of sonication for at least 1 h. Then 20 μL of the dispersion was drop-casted on a polished glassy carbon electrode (5 mm in diameter). Commercial Pt/C catalyst was obtained from Alfa Aesar (20% Pt on carbon black, HiSPEC 3000). The loading of Pt/C on RDE is 203 μg·cm^{-2}. After drying at room temperature, the catalyst-covered glassy carbon electrode was applied as the working electrode. Before the electrochemical tests, cyclic voltammetry was conducted at a scan rate of 50 mV·s^{-1} for at least 20 cycles with the potential range from 0 to −0.8 V to activate the catalysts under N_2 flow. Linear sweep voltammetry curves were collected at a scan rate of 10 mV·s^{-1} with a rotating rate of 1,600 rpm under O_2 flow. CV curves were measured at the potential range from 0.15 to 0.25 V vs. SCE at the scan rate of 5, 10, 20, 30, 40, and 50 mV·s^{-1}. For the conversion of potential against the reversible hydrogen electrode (RHE), the following equation (Eq. (1)) was applied

$$E_{RHE} = E_{SCE} + 0.059 \times pH + 0.244 \quad (1)$$

For the determination of H_2O_2 yield, the ring potential was set at 1.5 V. The electron transfer number (n) was calculated based on the following equations (Eqs. (1) and (2))

$$H_2O_2\% = I_r/(I_r + N \times I_d) \times 200 \quad (2)$$

$$n = (N \times I_d)/(I_r + N \times I_d) \times 4 \quad (3)$$

where I_d is the disk current, I_r is the ring current, and N (0.37) is the current collection efficiency of the Pt ring.

Acknowledgements

This work is supported by the National Natural Science Foundation of China (Nos. 21673150 and 51922073), Natural Science Foundation of Jiangsu Province (No. BK20180097). We acknowledge the financial support from the 111 Project, Collaborative Innovation Center of Suzhou Nano Science and Technology (NANO–CIC), the Priority Academic Program Development of Jiangsu Higher Education Institutions (PAPD). Y. Y. is grateful for the financial support from the UC-KIMS Center for Innovative Materials for Energy and Environment.

Electronic Supplementary Material: Supplementary material (additional experimental data, including TEM, SEM images and Table) is available in the online version of this article at https://doi.org/10.1007/s12274-020-3292-4.

References

[1] Hong, W. T.; Risch, M.; Stoerzinger, K. A.; Grimaud, A.; Suntivich, J.; Shao-Horn, Y. Toward the rational design of non-precious transition metal oxides for oxygen electrocatalysis. *Energy Environ. Sci.* **2015**, *8*, 1404–1427.

[2] Jiao, Y.; Zheng, Y.; Jaroniec, M.; Qiao, S. Z. Design of electrocatalysts for oxygen- and hydrogen-involving energy conversion reactions. *Chem. Soc. Rev.* **2015**, *44*, 2060–2086.

[3] Gewirth, A. A.; Varnell, J. A.; DiAscro, A. M. Nonprecious metal catalysts for oxygen reduction in heterogeneous aqueous systems. *Chem. Rev.* **2018**, *118*, 2313–2339.

[4] Yuan, X. L.; Jiang, X. J.; Cao, M. H.; Chen, L.; Nie, K. Q.; Zhang, Y.; Xu, Y.; Sun, X. H.; Li, Y. G.; Zhang, Q. Intermetallic PtBi core/ultrathin Pt shell nanoplates for efficient and stable methanol and ethanol electro-oxidization. *Nano Res.* **2019**, *12*, 429–436.

[5] Seh, Z. W.; Kibsgaard, J.; Dickens, C. F.; Chorkendorff, I.; Nørskov, J. K.; Jaramillo, T. F. Combining theory and experiment in electrocatalysis: Insights into materials design. *Science* **2017**, *355*, eaad4998.

[6] Zhu, Y. P.; Guo, C. X.; Zheng, Y.; Qiao, S. Z. Surface and interface engineering of noble-metal-free electrocatalysts for efficient energy conversion processes. *Acc. Chem. Res.* **2017**, *50*, 915–923.

[7] Indra, A.; Menezes, P. W.; Sahraie, N. R.; Bergmann, A.; Das, C.; Tallarida, M.; Schmeißer, D.; Strasser, P.; Driess, M. Unification of catalytic water oxidation and oxygen reduction reactions: Amorphous beat crystalline cobalt iron oxides. *J. Am. Chem. Soc.* **2014**, 136, 17530–17536.

[8] Hu, H.; Han, L.; Yu, M. Z.; Wang, Z. Y.; Lou, X. W. Metal-organic-framework-engaged formation of Co nanoparticle-embedded carbon@Co_9S_8 double-shelled nanocages for efficient oxygen reduction. *Energy Environ. Sci.* **2016**, *9*, 107–111.

[9] Yang, W. X.; Liu, X. J.; Yue, X. Y.; Jia, J. B.; Guo, S. J. Bamboo-like carbon nanotube/Fe_3C nanoparticle hybrids and their highly efficient catalysis for oxygen reduction. *J. Am. Chem. Soc.* **2015**, *137*, 1436–1439.

[10] Zhu, C. L.; Yin, Z. X.; Lai, W. H.; Sun, Y.; Liu, L. N.; Zhang, X. T.; Chen, Y. J.; Chou, S. L. Fe-Ni-Mo nitride porous nanotubes for full water splitting and Zn-air batteries. *Adv. Energy Mater.* **2018**, *8*, 1802327.

[11] Yan, X. C.; Jia, Y.; Yao, X. D. Defects on carbons for electrocatalytic oxygen reduction. *Chem. Soc. Rev.* **2018**, *47*, 7628–7658.

[12] Feng, S. Q.; Liu, C.; Chai, Z. G.; Li, Q.; Xu, D. S. Cobalt-based hydroxide nanoparticles@N-doping carbonic frameworks core–shell structures as highly efficient bifunctional electrocatalysts for oxygen evolution and oxygen reduction reactions. *Nano Res.* **2018**, *11*, 1482–1489.

[13] Huang, Z.; Pan, H. Y.; Yang, W. J.; Zhou, H. H.; Gao, N.; Fu, C. P.; Li, S. C.; Li, H. X.; Kuang, Y. F. *In situ* self-template synthesis of Fe–N-doped double-shelled hollow carbon microspheres for oxygen reduction reaction. *ACS Nano* **2018**, *12*, 208–216.

[14] Lv, L.; Zha, D. C.; Ruan, Y. J.; Li, Z. S.; Ao, X.; Zheng, J.; Jiang, J. J.; Chen, H. M.; Chiang, W. H.; Chen, J. et al. A universal method to engineer metal oxide–metal–carbon interface for highly efficient oxygen reduction. *ACS Nano* **2018**, *12*, 3042–3051.

[15] Su, C. Y.; Cheng, H.; Li, W.; Liu, Z. Q.; Li, N.; Hou, Z. F.; Bai, F. Q.; Zhang, H. X.; Ma, T. Y. Atomic modulation of FeCo–nitrogen–carbon bifunctional oxygen electrodes for rechargeable and flexible all-solid-state zinc–air battery. *Adv. Energy Mater.* **2017**, *7*, 1602420.
[16] Liu, X.; Liu, H.; Chen, C.; Zou, L. L.; Li, Y.; Zhang, Q.; Yang, B.; Zou, Z. Q.; Yang, H. Fe_2N nanoparticles boosting FeN_x moieties for highly efficient oxygen reduction reaction in Fe-N-C porous catalyst. *Nano Res.* **2019**, *12*, 1651–1657.
[17] Wu, K. L.; Chen, X.; Liu, S. J.; Pan, Y.; Cheong, W. C.; Zhu, W.; Cao, X.; Shen, R. A.; Chen, W. X.; Luo, J. et al. Porphyrin-like Fe-N_4 sites with sulfur adjustment on hierarchical porous carbon for different rate-determining steps in oxygen reduction reaction. *Nano Res.* **2018**, *11*, 6260–6269.
[18] Wang, Z. H.; Jin, H. H.; Meng, T.; Liao, K.; Meng, W. Q.; Yang, J. L.; He, D. P.; Xiong, Y. L.; Mu, S. C. Fe, Cu-coordinated ZIF-derived carbon framework for efficient oxygen reduction reaction and zinc–air batteries. *Adv. Funct. Mater.* **2018**, *28*, 1802596.
[19] Shen, M. X.; Wei, C. T.; Ai, K. L.; Lu, L. H. Transition metal–nitrogen–carbon nanostructured catalysts for the oxygen reduction reaction: From mechanistic insights to structural optimization. *Nano Res.* **2017**, *10*, 1449–1470.
[20] Tang, H. J.; Yin, H. J.; Wang, J. Y.; Yang, N. L.; Wang, D.; Tang, Z. Y. Molecular architecture of cobalt porphyrin multilayers on reduced graphene oxide sheets for high-performance oxygen reduction reaction. *Angew. Chem., Int. Ed.* **2013**, *52*, 5585–5589.
[21] Hu, B. C.; Wu, Z. Y.; Chu, S. Q.; Zhu, H. W.; Liang, H. W.; Zhang, J.; Yu, S. H. SiO_2-protected shell mediated templating synthesis of Fe–N-doped carbon nanofibers and their enhanced oxygen reduction reaction performance. *Energy Environ. Sci.* **2018**, *11*, 2208–2215.
[22] Jiang, R.; Li, L.; Sheng, T.; Hu, G. F.; Chen, Y. G.; Wang, L. Y. Edge-site engineering of atomically dispersed Fe–N_4 by selective C–N bond cleavage for enhanced oxygen reduction reaction activities. *J. Am. Chem. Soc.* **2018**, *140*, 11594–11598.
[23] Zheng, Y.; Jiao, Y.; Zhu, Y. H.; Cai, Q. R.; Vasileff, A.; Li, L. H.; Han, Y.; Chen, Y.; Qiao, S. Z. Molecule-level g-C_3N_4 coordinated transition metals as a new class of electrocatalysts for oxygen electrode reactions. *J. Am. Chem. Soc.* **2017**, *139*, 3336–3339.
[24] Tang, C.; Wang, H. F.; Zhang, Q. Multiscale principles to boost reactivity in gas-involving energy electrocatalysis. *Acc. Chem. Res.* **2018**, *51*, 881–889.
[25] Xia, W.; Mahmood, A.; Liang, Z. B.; Zou, R. Q.; Guo, S. J. Earth-abundant nanomaterials for oxygen reduction. *Angew. Chem., Int. Ed.* **2016**, *55*, 2650–2676.
[26] Wang, X. R.; Liu, J. Y.; Liu, Z. W.; Wang, W. C.; Luo, J.; Han, X. P.; Du, X. W.; Qiao, S. Z.; Yang, J. Identifying the key role of pyridinic-N–Co bonding in synergistic electrocatalysis for reversible ORR/OER. *Adv. Mater.* **2018**, *30*, 1800005.
[27] Zhao, W. S.; Li, G. D.; Tang, Z. Y. Metal-organic frameworks as emerging platform for supporting isolated single-site catalysts. *Nano Today* **2019**, *27*, 178–197.
[28] Zhao, M. T.; Huang, Y.; Peng, Y. W.; Huang, Z. Q.; Ma, Q. L.; Zhang, H. Two-dimensional metal–organic framework nanosheets: Synthesis and applications. *Chem. Soc. Rev.* **2018**, *47*, 6267–6295.
[29] Li, Z. H.; Shao, M. F.; Zhou, L.; Zhang, R. K.; Zhang, C.; Wei, M.; Evans, D. G.; Duan, X. Directed growth of metal-organic frameworks and their derived carbon-based network for efficient electrocatalytic oxygen reduction. *Adv. Mater.* **2016**, *28*, 2337–2344.
[30] Shang, L.; Yu, H. J.; Huang, X.; Bian, T.; Shi, R.; Zhao, Y. F.; Waterhouse, G. I. N.; Wu, L. Z.; Tung, C. H.; Zhang, T. R. Well-dispersed ZIF-derived Co,N-Co-doped carbon nanoframes through mesoporous-silica-protected calcination as efficient oxygen reduction electrocatalysts. *Adv. Mater.* **2016**, *28*, 1668–1674.
[31] Aijaz, A.; Masa, J.; Rösler, C.; Xia, W.; Weide, P.; Botz, A. J. R.; Fischer, R. A.; Schuhmann, W.; Muhler, M. Co@Co_3O_4 encapsulated in carbon nanotube-grafted nitrogen-doped carbon polyhedra as an advanced bifunctional oxygen electrode. *Angew. Chem., Int. Ed.* **2016**, *55*, 4087–4091.
[32] Xia, B. Y.; Yan, Y.; Li, N.; Wu, H. B.; Lou, X. W.; Wang, X. A metal–organic framework-derived bifunctional oxygen electrocatalyst. *Nat. Energy* **2016**, *1*, 15006.
[33] Hou, Y.; Wen, Z. H.; Cui, S. M.; Ci, S. Q.; Mao, S.; Chen, J. H. An advanced nitrogen-doped graphene/cobalt-embedded porous carbon polyhedron hybrid for efficient catalysis of oxygen reduction and water splitting. *Adv. Funct. Mater.* **2015**, *25*, 872–882.
[34] Wang, Q.; Shang, L.; Shi, R.; Zhang, X.; Zhao, Y. F.; Waterhouse, G. I. N.; Wu, L. Z.; Tung, C. H.; Zhang, T. R. NiFe layered double hydroxide nanoparticles on Co,N-codoped carbon nanoframes as efficient bifunctional catalysts for rechargeable zinc–air batteries. *Adv. Energy Mater.* **2017**, *7*, 1700467.
[35] Liu, S. H.; Wang, Z. Y.; Zhou, S.; Yu, F. J.; Yu, M. Z.; Chiang, C. Y.; Zhou, W. Z.; Zhao, J. J.; Qiu, J. S. Metal–organic-framework-derived hybrid carbon nanocages as a bifunctional electrocatalyst for oxygen reduction and evolution. *Adv. Mater.* **2017**, *29*, 1700874.
[36] Wang, X. J.; Feng, J.; Bai, Y. C.; Zhang, Q.; Yin, Y. D. Synthesis, properties, and applications of hollow micro-/nanostructures. *Chem. Rev.* **2016**, *116*, 10983–11060.
[37] Wang, J. Y.; Cui, Y.; Wang, D. Design of hollow nanostructures for energy storage, conversion and production. *Adv. Mater.* **2019**, *31*, 1801993.
[38] Mao, D.; Wan, J. W.; Wang, J. Y.; Wang, D. Sequential templating approach: A groundbreaking strategy to create hollow multishelled structures. *Adv. Mater.* **2019**, *31*, 1802874.
[39] Long, C. L.; Qi, D. P.; Wei, T.; Yan, J.; Jiang, L. L.; Fan, Z. J. Nitrogen-doped carbon networks for high energy density supercapacitors derived from polyaniline coated bacterial cellulose. *Adv. Funct. Mater.* **2014**, *24*, 3953–3961.
[40] Zhang, Q.; Zhang, T. R.; Ge, J. P.; Yin, Y. D. Permeable silica shell through surface-protected etching. *Nano Lett.* **2008**, *8*, 2867–2871.
[41] Zhang, Q.; Wang, W. S.; Goebl, J.; Yin, Y. D. Self-templated synthesis of hollow nanostructures. *Nano Today* **2009**, *4*, 494–507.
[42] Cai, Z. X.; Wang, Z. L.; Kim, J.; Yamauchi, Y. Hollow functional materials derived from metal–organic frameworks: Synthetic strategies, conversion mechanisms, and electrochemical applications. *Adv. Mater.* **2019**, *31*, 1804903.
[43] Tian, W.; Hu, H.; Wang, Y. X.; Li, P.; Liu, J. Y.; Liu, J. L.; Wang, X. B.; Xu, X. D.; Li, Z. T.; Zhao, Q. S. et al. Metal–organic frameworks mediated synthesis of one-dimensional molybdenum-based/carbon composites for enhanced lithium storage. *ACS Nano* **2018**, *12*, 1990–2000.
[44] Guan, B. Y.; Yu, L.; Lou, X. W. Formation of single-holed cobalt/N-doped carbon hollow particles with enhanced electrocatalytic activity toward oxygen reduction reaction in alkaline media. *Adv. Sci.* **2017**, *4*, 1700247.
[45] Feng, J.; Yin, Y. D. Self-templating approaches to hollow nanostructures. *Adv. Mater.* **2019**, *31*, 1802349.
[46] Zhao, Y. S.; Wan, J. W.; Yao, H. Y.; Zhang, L. J.; Lin, K. F.; Wang, L.; Yang, N. L.; Liu, D. H.; Song, L.; Zhu, J. et al. Few-layer graphdiyne doped with sp-hybridized nitrogen atoms at acetylenic sites for oxygen reduction electrocatalysis. *Nat. Chem.* **2018**, *10*, 924–931.
[47] Zhao, Y. S.; Tang, H. J.; Yang, N. L.; Wang, D. Graphdiyne: Recent achievements in photo- and electrochemical conversion. *Adv. Sci.* **2018**, *5*, 1800959.
[48] Zhao, Y. S.; Zhang, L. J.; Qi, J.; Jin, Q.; Lin, K. F.; Wang, D. Graphdiyne with enhanced ability for electron transfer. *Acta Phys. Chim. Sin.* **2018**, *34*, 1048–1060.
[49] Zhou, R. F.; Zheng, Y.; Jaroniec, M.; Qiao, S. Z. Determination of the electron transfer number for the oxygen reduction reaction: From theory to experiment. *ACS Catal.* **2016**, *6*, 4720–4728.
[50] McCrory, C. C. L.; Jung, S.; Peters, J. C.; Jaramillo, T. F. Benchmarking heterogeneous electrocatalysts for the oxygen evolution reaction. *J. Am. Chem. Soc.* **2013**, *135*, 16977–16987.
[51] Chen, J. N.; Yuan, X. L.; Lyu, F.; Zhong, Q. X.; Hu, H. C.; Pan, Q.; Zhang, Q. Integrating MXene nanosheets with cobalt-tipped carbon nanotubes for an efficient oxygen reduction reaction. *J. Mater. Chem. A* **2019**, *7*, 1281–1286.
[52] Yan, X. C.; Dong, C. L.; Huang, Y. C.; Jia, Y.; Zhang, L. Z.; Shen, S. H.; Chen, J.; Yao, X. D. Probing the active sites of carbon-encapsulated cobalt nanoparticles for oxygen reduction. *Small Methods* **2019**, *3*, 1800439.

[53] Zhao, S. L.; Yang, J.; Han, M.; Wang, X. M.; Lin, Y.; Yang, R.; Xu, D. D.; Shi, N. E.; Wang, Q.; Yang, M. J. et al. Synergistically enhanced oxygen reduction electrocatalysis by atomically dispersed and nanoscaled Co species in three-dimensional mesoporous Co, N-codoped carbon nanosheets network. *Appl. Catal. B* **2020**, *260*, 118207.

[54] Cheng, Q. Q.; Han, S. B.; Mao, K.; Chen, C.; Yang, L. J.; Zou, Z. Q.; Gu, M.; Hu, Z.; Yang, H. Co nanoparticle embedded in atomically-dispersed Co-N-C nanofibers for oxygen reduction with high activity and remarkable durability. *Nano Energy* **2018**, *52*, 485–493.

[55] Zhang, J. T.; Dai, L. M. Nitrogen, phosphorus, and fluorine Tri-doped graphene as a multifunctional catalyst for self-powered electrochemical water splitting. *Angew. Chem., Int. Ed.* **2016**, *55*, 13296–13300.

[56] Tao, L.; Qiao, M.; Jin, R.; Li, Y.; Xiao, Z. H.; Wang, Y. Q.; Zhang, N. N.; Xie, C.; He, Q. G.; Jiang, D. C. et al. Bridging the surface charge and catalytic activity of a defective carbon electrocatalyst. *Angew. Chem., Int. Ed.* **2019**, *58*, 1019–1024.

[57] Wang, J. Y.; Wan, J. W.; Wang, D. Hollow multishelled structures for promising applications: Understanding the structure–performance correlation. *Acc. Chem. Res.* **2019**, *52*, 2169–2178.

[58] Wang, L.; Wan, J. W.; Zhao, Y. S.; Yang, N. L.; Wang, D. Hollow multi-shelled structures of Co_3O_4 dodecahedron with unique crystal orientation for enhanced photocatalytic CO_2 reduction. *J. Am. Chem. Soc.* **2019**, *141*, 2238–2241.

[59] Wang, J. Y.; Tang, H. J.; Wang, H.; Yu, R. B.; Wang, D. Multi-shelled hollow micro-/nanostructures: Promising platforms for lithium-ion batteries. *Mater. Chem. Front.* **2017**, *1*, 414–430.

[60] Lyu, F.; Bai, Y. C.; Li, Z. W.; Xu, W. J.; Wang, Q. F.; Mao, J.; Wang, L.; Zhang, X. W.; Yin, Y. D. Self-templated fabrication of CoO–MoO_2 nanocages for enhanced oxygen evolution. *Adv. Funct. Mater.* **2017**, *27*, 1702324.